Robust absolute solar flux density calibration for the Murchison Widefield Array

Devojyoti Kansabanik [ID],[1] Surajit Mondal [ID],[2, 1] Divya Oberoi [ID],[1] Ayan Biswas [ID],[1] and Shilpi Bhunia [ID][3, 4, 5]

[1]*National Centre for Radio Astrophysics, Tata Institute of Fundamental Research, Pune University, Pune 411007, India*
[2]*Center for Solar-Terrestrial Research, New Jersey Institute of Technology, 323 M L King Jr Boulevard, Newark, NJ 07102-1982, USA*
[3]*Dublin Institute for Advanced Studies, Dublin, Ireland*
[4]*Trinity College, Dublin, Ireland*
[5]*Indian Institute of Science Education and Research, Pune, India*

ABSTRACT

Sensitive radio instruments are optimized for observing faint astronomical sources, and usually need to attenuate the received signal when observing the Sun. There are only a handful of flux density calibrators which can comfortably be observed with the same attenuation set up as the Sun. Additionally, for wide field-of-view (FoV) instruments like the Murchison Widefield Array (MWA) calibrator observations are generally done when the Sun is below the horizon to avoid the contamination from solar emissions. These considerations imply that the usual radio interferometric approach to flux density calibration is not applicable for solar imaging. A novel technique, relying on a good sky model and detailed characterization of the MWA hardware, was developed for solar flux density calibration for MWA (Oberoi et al. 2017; Mohan & Oberoi 2017). Though successful, this technique is not general enough to be extended to the data from the extended configuration of the MWA Phase II. Here we present a robust flux density calibration method for solar observations with MWA independent of the array configuration. We use different approaches – the serendipitous presence of strong sources; detection of numerous background sources using high dynamic range images in the FoV along with the Sun and observations of strong flux density calibrators with and without the additional attenuation used for solar observations; to obtain the flux scaling parameters required for the flux density calibration. Using the present method we have achieved an absolute flux density uncertainty $\sim 10\%$ for solar observations even in absence of dedicated calibrator observations.

1. INTRODUCTION

The quiet Sun is just about the source with highest flux density in the meter wavelength radio sky, and its flux density can increase by multiple orders of magnitude during the periods of active emissions. It is challenging to build sensitive radio instruments capable of providing a linear response spanning the entire range from the very faint astronomical sources of usual interest to the Mega-jansky solar bursts. Usually the low noise amplifiers, the very first elements in the signal chain, have sufficient dynamic range, but that does not hold true for the downstream signal chain. Solar observations, hence, typically require the use of *attenuators* early on in the signal path to bring down the signal levels sufficiently, so that they lie in the linear regime of the downstream signal chain. Since attenuators can bring down the signal level by multiple orders of magnitude, it becomes hard to observe other astronomical sources, including most of the so-called flux density calibrators, with this attenuation in place. Flux density calibrators are comparatively bright radio sources whose flux density and spectra are known accurately and are typically used for absolute flux density calibration (e.g Perley & Butler 2017). The standard flux density calibrator observations are gener-

Corresponding author: Devojyoti Kansabanik
dkansabanik@ncra.tifr.res.in

ally done without any additional attenuators. Transferring the flux density calibration determined using observations of standard flux density calibrators to the Sun, generally observed with attenuators, is not straight forward and requires a detailed and accurate characterisation of the attenuators. It is very effort intensive to do this characterization, and in practice, it is rarely available. This is also the case with the Murchison Widefield Array (MWA; Lonsdale et al. 2009; Tingay et al. 2013).

Solar absolute flux density calibration usually relies on the use of the few very bright sources whose flux density is large enough for them to be observed using the same attenuation setting as solar observations. This approach is followed at the Nançay Radio Heliograph (NRH; e.g. Bonmartin et al. 1983; Avignon et al. 1989), the Gauribidanur Radio Heliograph (GRH; e.g. Sundaram & Subramanian 2004, 2005) and the Low Frequency Array (LOFAR; e.g. Breitling et al. 2015; Kontar et al. 2017). Conventionally, calibrator observations are scheduled to be observed adjacent to and/or interspersed with observations of the target source(s). This is done to minimise the impacts of any drifts in instrumental gains in the time between observations of the calibrator and target source(s). The wide field-of-view (FoV) and high primary beam sidelobes of the MWA imply that observations of flux density calibrators while the Sun is above the horizon can have significant contamination from the solar signal. Hence at the MWA, the practice has been to observe the flux density calibrators before sunrise and after sunset and, to broaden the pool of suitable calibrators, without the use of any additional attenuation. Additionally, during the early periods of MWA solar observations (2013 July to 2014 April), no calibrator observations in the same spectral configuration as the solar observations are available, further complicating the task of absolute flux density calibration for these observations.

Taking advantage of the facts that the MWA is a very well characterized instrument, including a well modelled primary beam, and the availability of reliable sky models (e.g. Haslam et al. 1982), Oberoi et al. (2017) implemented an innovative and computationally lean non-imaging technique for absolute solar flux density calibration. They estimated that the uncertainty in the absolute flux density estimates obtained using this technique generally lie in the range $10 - 60\%$. Suresh et al. (2017) and Sharma et al. (2018) used it successfully to get reliable flux density calibration for non-imaging studies. Mohan & Oberoi (2017) presented a technique to transfer this to interferometric images which has been used in multiple works (e.g. Mondal et al. 2019; Mohan et al. 2019b,a; Mondal et al. 2020b; Sharma & Oberoi

2020; Mohan 2021). Though successful, this technique relied crucially on the availability of multiple very short baselines ($\lesssim 10\lambda$) to obtain the total solar flux density and also to average over baseline-to-baseline fluctuations arising largely from manufacturing tolerances. In its Phase II, the MWA now has multiple configurations (Wayth et al. 2018). The extended configuration of MWA Phase II, which offers the highest angular resolution and is more desirable from a solar imaging perspective, has few baselines short enough to meet the criterion imposed by Oberoi et al. (2017). An independent approach has also been used in the past to calibrate flux density of the solar MWA data (e.g. McCauley et al. 2017; Rahman et al. 2019, etc.). In this approach the solar maps obtained using the MWA data are scaled such the integrated solar flux density matches the prediction of data driven models like FORWARD (Gibson et al. 2016). Limitations of this technique has been discussed in Sharma & Oberoi (2020) and mainly stem from the inadequacies of the model.

With improved imaging quality now available from instruments like the MWA, the need for a precise solar flux density calibration has also become evident. Applications requiring precise flux density calibration include – (1) modeling of the gyrosynchrotron emission from the Coronal Mass Ejection (CME) plasma to estimate physical parameters of CMEs (e.g. Bastian et al. 2001; Tun & Vourlidas 2013; Carley et al. 2017; Mondal et al. 2020b); and (2) attempts at detailed comparison of the radio observable, including flux densities, obtained from elaborate models implemented by tools like FORWARD (Gibson et al. 2016) with the radio maps from the MWA (Sharma & Oberoi 2020).

The aim of this work to use multiple independent approaches to perform robust absolute solar flux density calibration across MWA frequency range. The approaches explored here include – (1) Using the serendipitous presence of a strong source of known flux density in the range of few hundreds of Jansky, in the wide FoV of MWA during solar observations; (2) Using the high quality imaging delivered by the recently developed Automated Imaging Routine for Compact Array for Radio Sun (AIRCARS; Mondal et al. 2019, Kansabanik D. et al. in preparation) to detect numerous galactic and extra-galactic background sources with flux densities in the range from a few to a few tens of Jansky in the wide FoV of the MWA during solar observation. The flux densities of these sources are known independently from the GLEAM survey (Wayth et al. 2015; Hurley-Walker et al. 2017); and (3) Observations of a strong flux density calibrator source with and without the additional attenuation. Using these approaches and a database of MWA

calibration solutions which has recently been made available (Sokolowski et al. 2020), we develop a flux density calibration scheme useful for all solar observations with the MWA.

This paper is organised as follows: Section 2 describes the observations and data analysis, and Section 3 presents the results, including a comparison of the solar imaging quality with the GLEAM survey. It is followed by a short Section 4 describing the method to apply the flux scaling parameters to any solar observation, and finally the conclusions in Section 5.

2. OBSERVATIONS AND DATA ANALYSIS

We have analysed 4 datasets which were recorded with the MWA on 2014 May 04, 2014 July 12, 2014 September 28 and 2020 June 20. These were observed under the proposal code G0002. We refer to these observations by their observation dates, 20140504, 20140712, 20140928 and 20200620, in the following text. The details of these observations are given in Table 1. For 20140928, data corresponding to frequencies above 132 MHz were bad and had to be discarded. The spectral setting of "picket fence" refers to a spectral configuration where the 30.72 MHz of observing bandwidth is distributed in 12 sub-bands each of width 2.56 MHz, centered close to 80, 88, 96, 108, 120, 132, 145, 160, 196, 210, 218 and 240 MHz. Each of these sub-bands are called 'picket'. In the contiguous mode, we observe the band from ∼119–151 MHz. All of the observations were done using channel widths of 40 kHz and a time resolution of 0.5 second. The observations on 2014 May 04, 2014 September 28 and 2020 June 20 are solar observations, while VirgoA observations on 2014 July 12 were done at night time.

2.1. *Approach to solar calibration and imaging*

Conventionally, for interferometric imaging one needs to determine the complex gains of the individual antennas of the array. The process of determining the amplitude part of these gains using observations of sources whose flux density and spectra are known *a-priori*, the so called flux density calibrator sources, is referred to as flux density calibration. The same observations are used to determine the phase part of the complex gains to make the array coherent. The phase solutions are further refined using observations of compact sources in the vicinity of the field of interest, the so called phase calibrators, and finally the process of self-calibration.

Making use of the compact and centrally condensed array configuration of the MWA and the very high flux density of the Sun, one can devise robust algorithms to determine the phases of the antenna gains without requiring any calibrator observations. A relative calibration, across both antennas and bandwidth, of the

amplitudes of the antenna gains can also be easily done. AIRCARS implements this primary idea with many refinements and optimizations for snapshot spectroscopic solar imaging with the MWA. As AIRCARS does not rely on observations of flux density calibrators, it cannot provide images on an absolute flux density scale and is limited to providing relative bandpass amplitude calibration every 1.28 MHz for the antenna gains. This work provides a robust prescription for obtaining absolute flux density calibrated solar radio images for the MWA, even in absence of observations of suitable flux density calibrators and irrespective of the array configuration used.

2.2. *Data analysis for 20140928 and 20200620*

For these observations, the data analysis was fairly straight forward as the sources of interest, Crab and VirgoA, are of comparable surface brightness to the quiet Sun (Perley & Butler 2017). The data were imaged using AIRCARS (Mondal et al. 2019). The data quality for 20140928 are bad above 145 MHz and not used here. While the spectral sampling of calibration scans were matched to solar observations, the calibrator sources were observed without the additional signal attenuation used for solar observations. Hence, for these observations, no fluxscale is derived from calibrator observations. An independent relative self calibration is performed for each of the coarse channels to determine normalized gain solutions. Appropriate masks were used to ensure that both the Sun and Crab/VirgoA were "cleaned" and included in the model used for self-calibration. The image of Virgo-A and Crab with the Sun in the FoV are shown in Figure 1. We used different temporal averaging for different datasets and listed in Table 1. All other AIRCARS parameters were left at their default values. After the final images were obtained, imfit task available in the Common Astronomical Software and Analysis (CASA, Mc-Mullin et al. 2007) was used to estimate the flux density of these sources. Crab could be fitted well with a single Gaussian with residual flux density $< 3\%$. For these two epochs we have reliable images for frequencies < 145 MHz. At these low-frequencies VirgoA can also be modeled with a small number of Gaussians components with a residual flux density $< 4\%$. No significant emission feature is seen in either of the residual images. The flux-scaling factor for reference epochs (Table 1, $F_{ref}(\nu) = F_{cat}(\nu)/F_{app,ref}(\nu)$, was computed by comparing the obtained primary beam corrected apparent integrated flux density, $F_{app,ref}(\nu)$, with the values, $F_{cat}(\nu)$, available from NASA/IPAC Extrgalac-

Label	Date	Attenuator settings (dB)	Array configuration	Spectral mode	Sun in FoV	Source(s) used	Imaging bandwidth (MHz)	Imaging integration time (s)
20140504	2014 May 04	10	Phase I	Picket fence	Yes	Multiple faint sources	2.56	120
20140712	2014 July 12	10	Phase I	Picket fence	No	Virgo A	2.56	0.5
20140928	2014 September 28	14	Phase I	Picket fence	Yes	Virgo A	0.16	0.5
20200620	2020 June 20	10	Phase II extended	Contiguous	Yes	Crab	0.16	9

Table 1. Details of the different observations used.

tic Database[1] or from GLEAM catalogue. The primary beam correction was obtained using the model by Sokolowski et al. (2017). We calculate the uncertainty on $F_{ref}(\nu)$, $\Delta F_{ref}(\nu)$, by considering only the errors on the measured flux densities from the image. It is given by $\Delta F_{ref}(\nu) = F_{ref}(\nu) \times \Delta F_{intg}(\nu)/F_{intg}(\nu)$ where $F_{intg}(\nu)$ and $\Delta F_{intg}(\nu)$ are the integrated flux density of the source and the uncertainty on it respectively. We note that the noise in the final radio image follows a Gaussian distribution before a correction for the primary beam is applied. However, quantities like $F_{ref}(\nu)$ and $\Delta F_{ref}(\nu)$ can only be computed after correcting for the primary beam. Hence, the distribution of $\Delta F_{ref}(\nu)$ is not expected to follow a Gaussian as is discussed in Sec. 3.1.

2.3. Data analysis for 20140504

As none of the sources in the FoV were strong enough to be detectable in snapshot images in presence of the Sun and the solar attenuation, this dataset required significantly more involved analysis than the other three. Some of the requirements of this analysis were not met by AIRCARS in its original form. AIRCARS had focused primarily on the spectroscopic snapshot imaging use case. As it was always working with only one spectral channel at a time, AIRCARS did not need relative bandpass calibration capability. Detecting the much fainter background sources, however, requires averaging over the entire 2.56 MHz bandwidth of the spectral pickets. Since the instrumental bandpass amplitude and phase is not constant over frequency, we require bandpass calibration before making the image over 2.56 MHz. The large difference between the observation times of calibrator sources and the Sun can potentially lead to changes in shapes of the bandpass amplitudes and phases between the calibrator and target sources.

We perform independent *relative* bandpass calibration for each 2.56 MHz picket, but do not determine any *absolute* bandpass gain to account for the variation in spectral gain across the MWA band spanned by the pickets.

2.3.1. *Imaging the faint sources*

To overcome the limitations just mentioned, AIRCARS was augmented to include bandpass self-calibration. This is a part of a larger effort to develop the next and more capable incarnation of AIRCARS and will be presented in detail in a forthcoming paper (Kansabanik D. et al., in preparation). The bandpass self-calibration required us to find a way to deal with the degeneracy between the instrumental bandpass shape and the intrinsic spectral structure of the source (Sun). For convenience we assume that the spectral structure of the Sun to be flat over the calibration bandwidth of 2.56 MHz. These data come when the Sun was quiet (Fig. 2). The quiet Sun metrewave radio emission arises due to bremstrahluung from the million Kelvin coronal plasma. As the optical depth of this plasma approaches unity, a blackbody spectrum is an acceptable approximation. The blackbody spectrum departs from a flat one by $\lesssim$ 5% over a fractional bandwidth of $\lesssim$ 2.5%. Hence ignoring the spectral variation over our narrow bandwidths of observation is a reasonable assumption.

The basic approach was to image and model the solar emission, subtract it from the observed visibilities and image the residual visibilities to look for the background sources. This was implemented as follows – augmented AIRCARS was used to generate a solar image integrated over the full 2.56 MHz bandwidth of each spectral picket at 10 s resolution. This solar emission was modeled using the CASA *tclean* task without the *w-projection* algorithm switched on. A mask which limited the cleaning only to the solar disc was used. The final solar images and clean models were generated and the model visibilities for the Sun corresponding to the clean model were subtracted from the calibrated visibil-
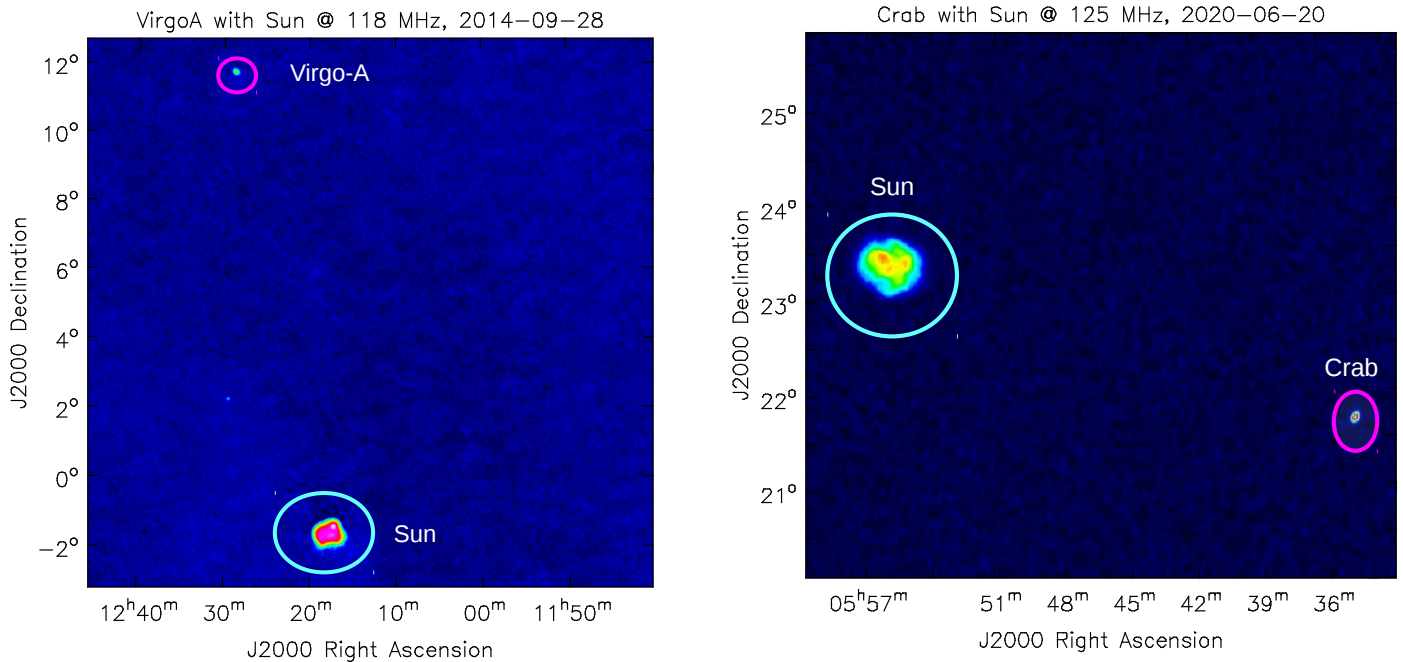
---

[1] https://ned.ipac.caltech.edu

Figure 1. Left panel : A map at 118 MHz showing Virgo-A and the Sun. Right panel : A map at 125 MHz showing Crab and the Sun.
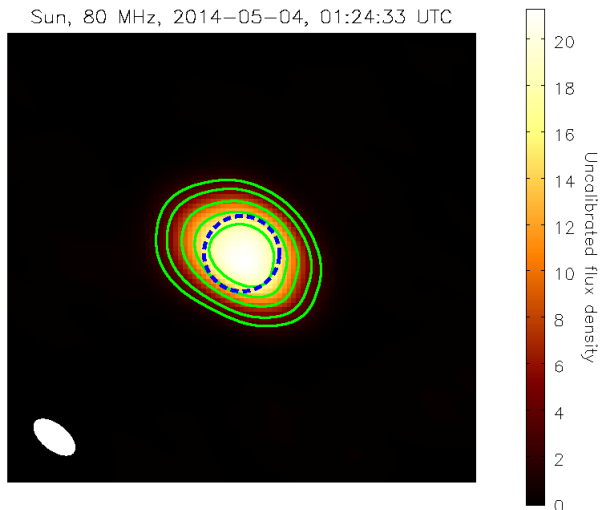

Figure 2. A map of the radio Sun at 80 MHz. The green contours are at 0.1, 0.2, 0.4, 0.6, 0.8 of the peak flux density. The blue dashed circle represents the optical disc of the Sun and the point spread function is shown by the ellipse at the bottom left.

ities using the CASA *uvsub* task. The residual visibilities thus obtained over the 2 minute were imaged using the CASA *tclean* task with the *w-projection* algorithm switched on and with uniform weighting. While imag-

ing the residuals visibilities, the phase centre was shifted close to the direction of the peak of the primary beam.

2.4. *Data analysis for 20140712*

These observations were designed to look at a strong calibrator with and without the attenuation usually used for solar observations and were done at night. For this observation, since the Sun was not present in the field of view, the analysis was straight forward. We follow similar approach of calibration as done in AIRCARS. Each of the 12 bands of width 2.56 MHz was calibrated using normalised bandpass of the each sub-band using the *bandpass* task of CASA (McMullin et al. 2007) for every 10 s time interval. This Imaging was done for each of these 12 bands. At higher frequencies VirgoA is resolved by the MWA baselines. Hence "Python Blob Detector and Source Finder" (PyBDSF; Mohan & Rafferty 2015) was used to fit multiple Gaussians to it, and the sum of flux densities of all the Gaussian components was regarded as the total flux density of VirgoA. We used the VirgoA flux densities from Perley & Butler (2017) to obtain $F_{ref}(\nu)$ using the primary beam corrected values obtained from the 2.56 MHz images.

3. RESULTS
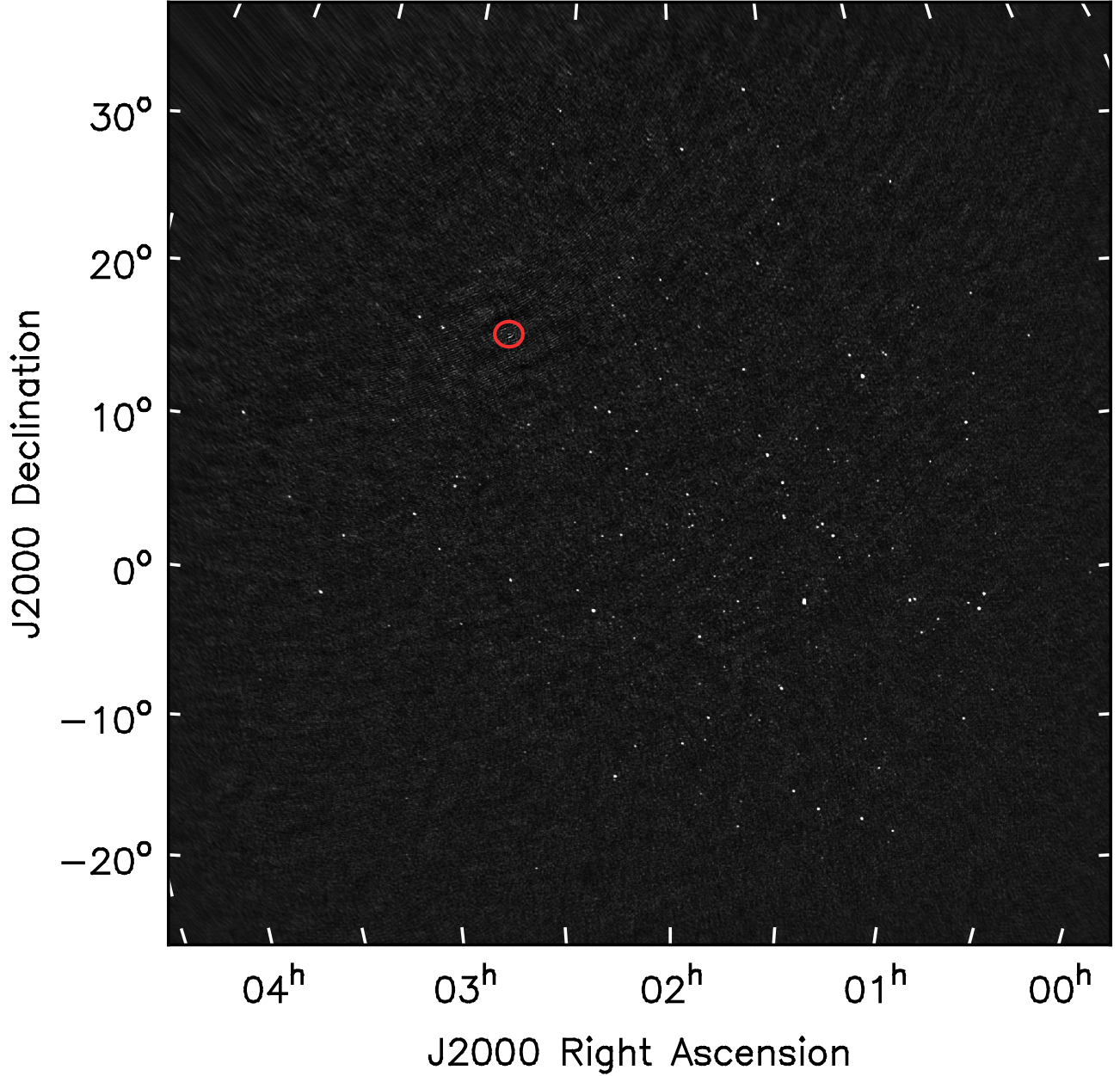
3.1. *Determining F_{ref} from weak sources*

Figure 3. Image centred at 80 MHz; $\sim 60°$ in each side; obtained over 2 minutes and 2.28 MHz after subtraction of modelled solar visibilities from the data. The image is from the observation on 2014 May 04 and the red circle with radius 2 $R_\odot$ is the region where the Sun was present.

A prerequisite for determining $F_{ref}(\nu)$ is to either have one or more strong flux density calibrator sources in the FoV or several weak sources so that the fluctuations due uncertainty on individual estimates of $F_{ref}(\nu)$ can get averaged out. Naturally, detecting weak sources is more challenging and, to the best of our knowledge, imaging of multiple background sources in the vicinity of the Sun is yet to be demonstrated at metre wavelengths. Figure 3 is perhaps the first image to show detection of numerous background sources with high signal-to-noise at low radio frequencies. The closest source to the Sun is at ~ 20 $R_\odot$ with a flux density 4.9 Jy. The $F_{ref}(\nu)$ obtained for different sources from 20140504 observation is shown in Figure 4. No systematic variation of $F_{ref}(\nu)$ with primary beam is apparent. All results stated here come from the observations on 20140504 and unless otherwise mentioned, correspond to 80 MHz. Dy-

namic range of the images at other frequencies below 145 MHz are comparable.

Images at all frequencies were searched for sources independently before primary beam correction using the source finding software PyBDSF (Mohan & Rafferty 2015). PyBDSF was tuned such that only sources with at least a 7σ significance, where σ is the local rms in the image as calculated by PyBDSF, were selected. The local rms is expected to drop with increasing angular distance from the Sun and was found to vary by a factor of about 2 across the FoV. It was also ensured that none of the sources included any pixels with flux density below 5σ. No sources were detected at frequencies above 145 MHz. We attribute this to the combined effects of the flux density of the sources dropping at higher frequencies due to their typical negative spectral indices ($S_\nu \propto \nu^\alpha$) and the increasing solar flux density leading to higher system temperature (and lower sensitivity) at higher frequencies. In addition, the area of the FoV also decreases with increasing frequency. Additionally the data quality was much poorer above 145 MHz. The sensitivity achieved here fell short of what was needed for detection of sources with sufficient signal-to-noise at higher frequencies.

All of the detected sources were carefully examined visually. To avoid possible impacts of differences in the sensitivities of the images on extended low surface brightness features on $F_{ref}(\nu)$ estimates, we use only unresolved sources. The detected compact sources were cross matched with the MWA GLEAM survey catalogue (Hurley-Walker et al. 2017). Cross-matching was done using *Aladin* (Bonnarel et al. 1999), assuming that the sources can at most shift by $20'$ from their reference positions. The choice of maximum allowed shift was motivated by visual inspection of the sources detected in our image and the GLEAM sources. This shift can occur due to multiple reasons including the following.

1. The calibrator observations were carried out at night while these observations come from close to solar transit. The refractive shift estimated and corrected for by the calibrator many hours apart and in a different direction are not be applicable for solar observation. In addition, the process of self-calibration can also introduce an artificial direction independent shift in the source locations. Both these effects contribute to giving rise to a direction independent shift in the source locations.

2. Night time direction dependent refractive shifts due to ionospheric structures have already been convincingly demonstrated (e.g. Loi et al. 2015; Loi et al. 2015; Jordan et al. 2017; Hurley-Walker & Hancock 2018; Helmboldt & Hurley-Walker 2020, etc.). The day time ionosphere can have about an order of magnitude higher electron column density. It is hence reasonable to expect significant direction dependent shifts due to ionospheric refraction.

Cross-matching catalogues which have been observed with different resolutions can be tricky. GLEAM survey data used here was done with the MWA Phase I by observing the fields close to transit. In case of 20140504, the solar elevation was $31.3°$ and hence the angular resolution is poorer than that of GLEAM. Conventionally under such circumstances, only the sources which are unresolved in both images are used. To avoid loosing the sources unresolved in our images but resolved in GLEAM, we pursue an approach inspired by Rogers et al. (2004). Sources which produce a single match in the GLEAM catalogue and remain unresolved in GLEAM pose no challenge. Instances when a single unresolved source in our images matches more than one sources in GLEAM catalogue require some thought. In such instances, we regard the integral of flux densities inside a region of the size of the point spread function (PSF) of our image centred on the brightest of the matched GLEAM sources as the effective flux density of the source. We have verified that the results obtained following this procedure and those obtained using unique unresolved GLEAM sources are consistent.

The GLEAM flux density at our frequency of interest is obtained by linear interpolation of flux densities measured by GLEAM at the frequency bands straddling the frequency of interest. Within the FWHM of the primary beam, we can detect all sources above a GLEAM flux density threshold of 10 Jy at 80 MHz. The sensitivity levels are comparable at other frequencies. At location where the primary beam gain is higher, we can detect much fainter sources. The weakest detected source had a GLEAM flux density of 4.6 Jy at 80 MHz near the peak of the primary beam. As we use a 7σ threshold for choosing the sources, this implies that close to the peak of the primary beam, the image rms is approximately 0.6 Jy.

Another issue to remain mindful of is the variability of flux densities (Bell et al. 2013; Rowlinson et al. 2016; Lynch et al. 2017). In order to avoid incurring errors in $F_{ref}(\nu)$ estimation by using sources with time variable flux densities, only sources for which the estimated $F_{ref}(\nu)$ lies between the 10th and 90th percentile are used. This criteria is met by 81 of the detected sources and their locations are shown in Figure 4. The $F_{ref}(\nu)$ determined from each of these sources, the primary beam gain at their locations and the observed
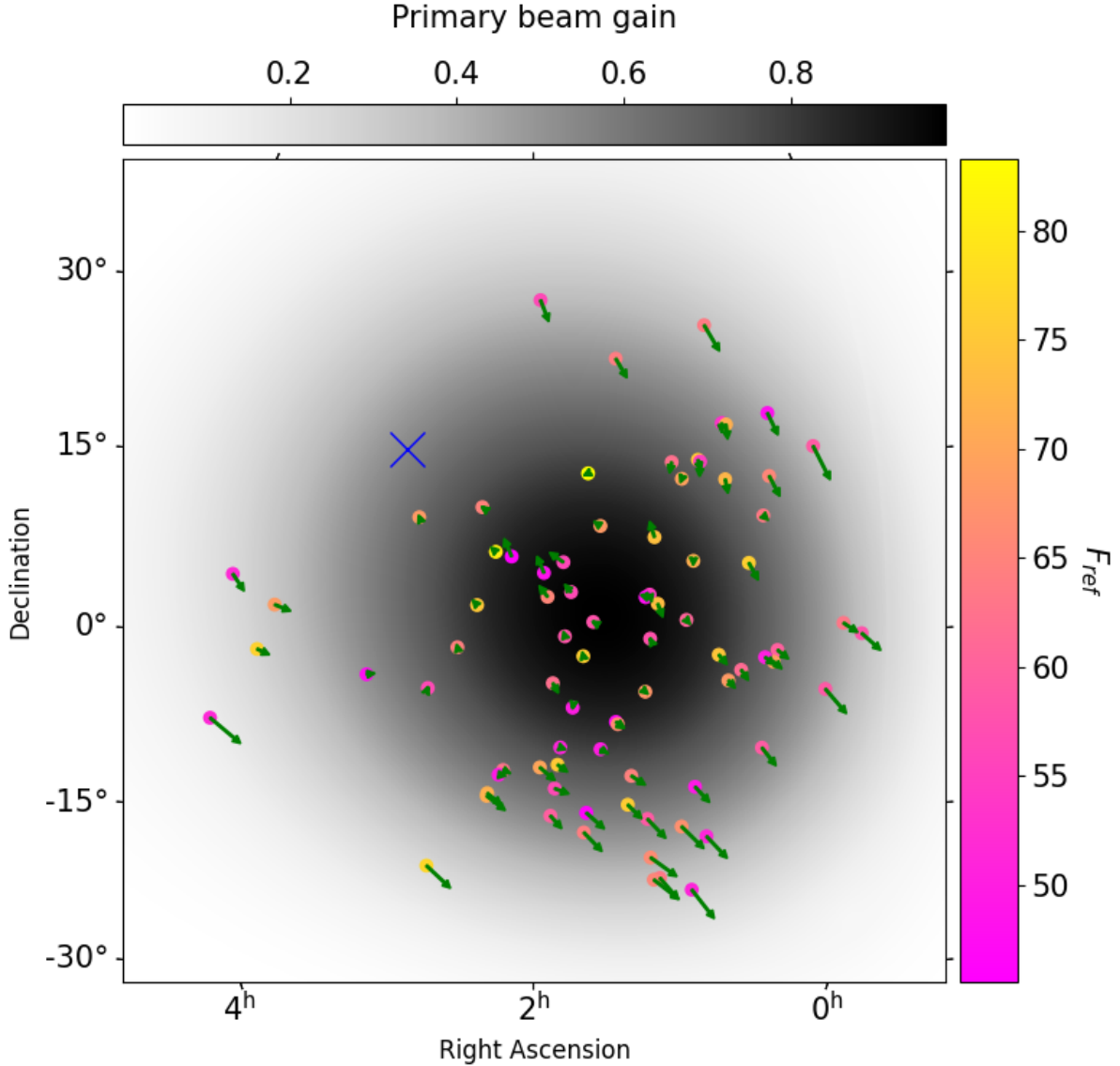
Figure 4. The location of the subset of detected sources from observation on 2014 May 04 used for determining $F_{ref}(\nu)$ are shown by colored dots. The colors of the dots denote their flux scaling factor determined for each of the sources and the primary beam gain at those locations is shown by the background grey scale. The arrows mark the shift of these source from their GLEAM catalogue positions, multiplied by a factor of 15 to make them visible. The location of the Sun is shown by blue cross mark.

shifts from their GLEAM catalogue positions are also shown in the Figure 4. The vectors showing the observed shifts of neighboring sources tend to be similar and vary smoothly across the large FoV. This systematic variation across the image is consistent with an ionospheric origin (Loi et al. 2015; Loi et al. 2015; Jordan et al. 2017; Hurley-Walker & Hancock 2018; Helmboldt & Hurley-Walker 2020).

The left panel of Figure 5 shows $F_{ref}(\nu)$ estimated from individual sources, along with the associated un-

certainty, as a function of their GLEAM flux densities. Since the rms noise in the GLEAM images are much smaller than that of our image (Appendix A), the contribution of error in GLEAM flux densities to $\Delta F_{ref}(\nu)$ is small and has been ignored. $\Delta F_{ref}(\nu)$ is calculated as mentioned in Section 2.2.

The middle panel of Fig. 5 shows the histogram of $F_{ref}(\nu)$. The observed spread in the histogram results from the intrinsic uncertainties in the values of $F_{ref}(\nu)$ determined for each of the sources. Using all sources at
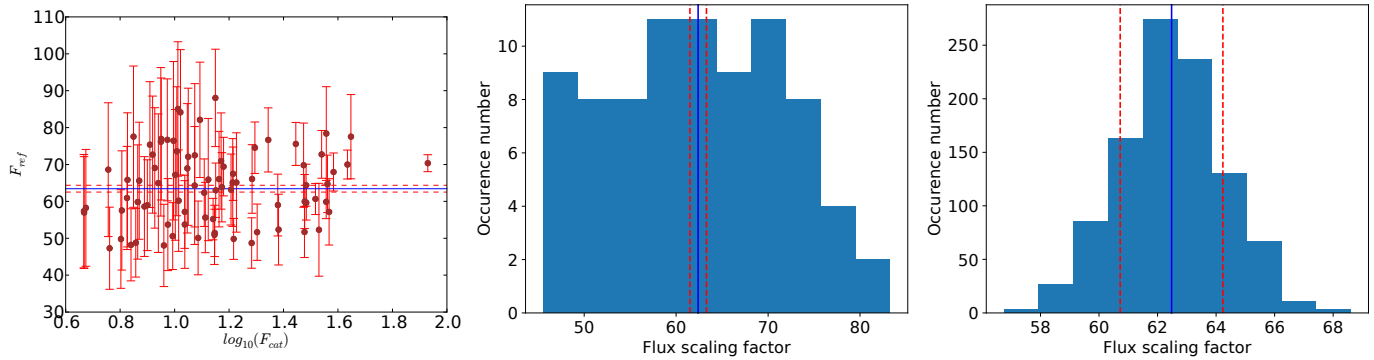
Figure 5. Left panel: Estimated $F_{ref}(\nu)$ against the logarithm of GLEAM flux density, $log_{10}(F_{cat})$, for individual sources at 80 MHz. Middle panel: Histogram of reference flux scaling factors, $F_{ref}(\nu)$. Left panel: Histogram of $F_{ref}(\nu)$ obtained from random sampling. The blue solid line shows the median scaling factor and the red dashed lines the 1σ uncertainty.
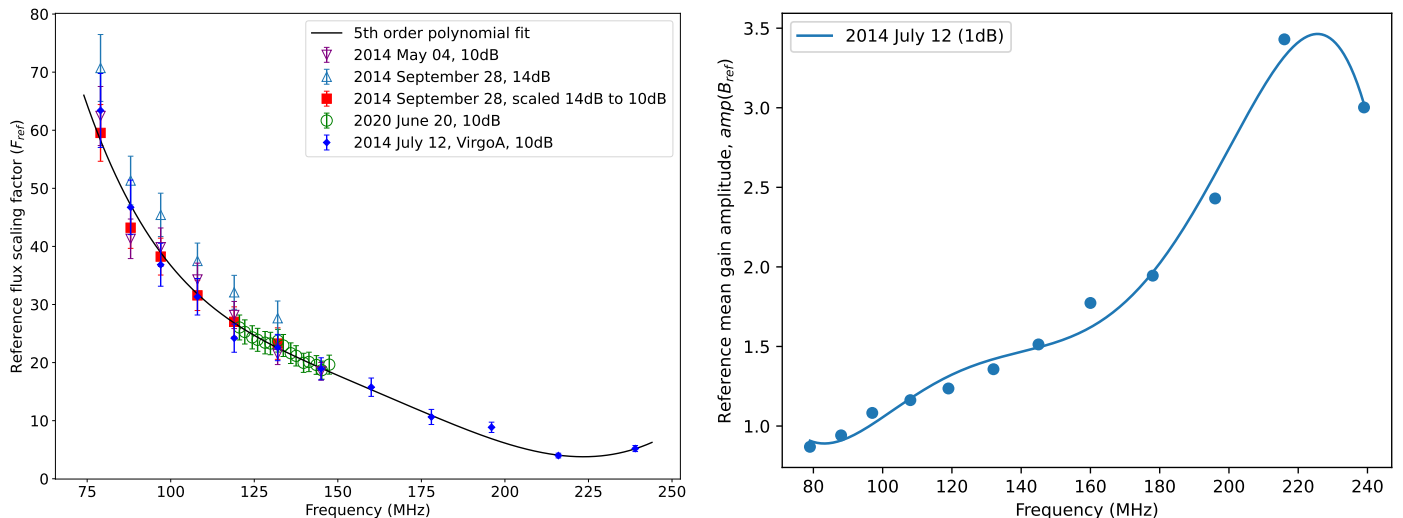

Figure 6. Left panel : The reference flux scaling factor, $F_{ref}(\nu)$, obtained for different observations. The black line shows the fitted polynomial. Right panel : Mean reference bandpass amplitude, $amp\,(B_{ref})$, for 2014 July 12.

80 MHz, the inverse variance weighted mean of $F_{ref}(\nu)$ is found to be 62.4 ± 0.9.

As discussed in Sec. 2.2, the distribution of ΔF_{ref} is not expected to follow a Gaussian. The noise characteristics of the image itself were Gaussian before the primary beam correction, so it is reasonable to expect the estimated uncertainty on each of the individual values of F_{ref} determined to be drawn from their own Gaussian distribution – one with a mean and sigma corresponding to $F_{ref}(\nu)$ and $\Delta F_{ref}(\nu)$ respectively. As a consistency check, a thousand sets were created, each with a value drawn from a Gaussian distribution with a mean and rms equal to $F_{intg}(\nu)$ and $\Delta F_{intg}(\nu)$, corresponding to each of the sources used. The mean $F_{ref}(\nu)$ was then computed for each of these 1000 sets. The right panel

of Fig. 5 shows the histogram of the mean $F_{ref}(\nu)$ from these thousand sets, which shows a well defined Gaussian. This approach yields a $F_{ref}(\nu)$ of 62 ± 2 at 80 MHz. This exercise makes it evident that there are no systematic errors associated with the determination of $F_{ref}(\nu)$, which otherwise would show as a departure from Gaussian distribution. This also verifies that the inverse variance weighted mean of the F_{ref} shown in the left panel is consistent with estimate from this exercise.

3.2. Flux scale parameters

In this section we discuss about the origin of different flux density scaling parameters and how they are derived.

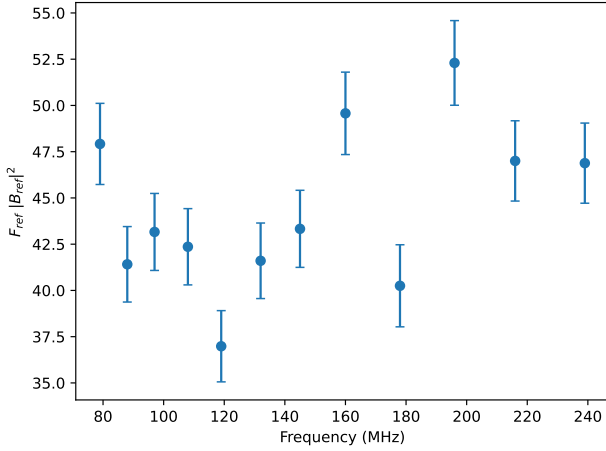#### 3.2.1. Formulating flux scale parameters

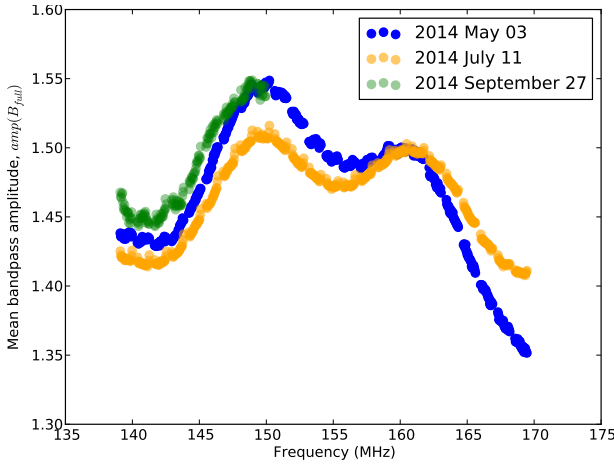**Figure 7.** Variation of product of $F_{ref}(\nu)$ and $|B_{ref}(\nu)|^2$ with frequency.

Figure 8. Mean bandpass amplitudes, $amp\ (B_{full})$, for the calibrator observations. Three colors represent three observing epochs.

It is common practice in radio interferometric calibration to decompose the *antenna dependent* instrumental bandpass gain, $B_{tot}(t,\ \nu)$ into a purely time dependent part, $G_{mean}(t)$, and, a purely frequency dependent part $B_{full}(\nu)$. Following this approach we decompose, $B_{tot}(\nu,t)$ as follows:

$$B_{tot}(\nu,\ t) = G_{mean}(t)\ B_{full}(\nu). \tag{1}$$

In the case of solar observations with the MWA, the conventional approach of flux density calibration is not followed, as has been discussed in Section 2.1. This section provides the prescription to implement Eq. 1 for the MWA solar observation.

AIRCARS performs spectrally local bandpass calibration, normalised to unity, for each 2.56 MHz picket. The

MWA has a significant variation in its response across the band which is not taken into account by the bandpass calibration done by AIRCARS. To take the bandapss gain variation across pickets into account we decompose $B_{full}(\nu)$ into picket bandpass, $B_{picket}(\nu)$, and the inter picket bandpass, $B_{inter}(\nu)$ both normalised to unity

$$B_{full}(\nu) = B_{picket}(\nu)\ B_{inter}(\nu) \tag{2}$$

Equation 1 then can then be expressed as:

$$B_{tot}(\nu,t) = G_{mean}(t)\ B_{picket}(\nu)\ B_{inter}(\nu). \tag{3}$$

Of these $B_{picket}(\nu)$ is already applied by AIRCARS. AIRCARS computes and corrects for $B_{picket}(\nu)$ when we use imaging over a picket of 2.56 MHz. When imaging over much narrower bandwidth of 160 kHz, we simply assume $B_{picket}(\nu) = 1$ as bandpass is essentially flat over this tiny band. Only the two remaining terms need to be computed and corrected for. Thus we can express $B_{tot}(\nu,\ t)$ as,

$$B_{tot}(\nu,\ t) = G_{mean}(t)\ B_{inter}(\nu) \tag{4}$$

To determine these parameters, we use the catalogue flux densities, $F_{cat}(\nu)$, of the background galactic and extra-galactic sources. Before comparing the observed flux densities with $F_{cat}(\nu)$, the images are corrected for the primary beam response. The flux densities observed in these primary beam corrected images are referred to as $F_{app}(\nu,t)$, the apparent flux density, which can differ from epoch to epoch. In addition, for solar observations, we also need to account for the effect of the attenuators, $A(\nu,t)$, which in the most general case will be a function of time and frequency. $F_{app}(\nu,t)$ can then be expressed in terms of $F_{cat}(\nu)$, $B_{tot}(\nu,t)$ and $A(\nu,t)$ using Eqs. 1 and 4 as :

$$
\begin{aligned}
F_{app}(\nu,t) &= A(\nu,t)\ |B_{tot}(\nu,t)|^2\ F_{cat}(\nu) \\
&= A(\nu,t)\ |G_{mean}(t)|^2\ |B_{full}(\nu)|^2\ F_{cat}(\nu) \\
&= A(\nu,t)\ |G_{mean}(t)|^2\ |B_{inter}(\nu)|^2\ F_{cat}(\nu) \\
\frac{F_{cat}(\nu)}{F_{app}(\nu,\ t)} &= \frac{1}{A(\nu,\ t)\ |G_{mean}(t)|^2\ |B_{inter}(\nu)|^2} \\
F_{scale}(\nu,\ t) &= \frac{1}{A(\nu,\ t)\ |G_{mean}(t)|^2\ |B_{inter}(\nu)|^2} \\
F_{scale}(\nu,\ t) &= \frac{1}{A(\nu,\ t)\ |B_{tot}(\nu,t)|^2}
\end{aligned}
\tag{5}
$$

We regard observations on all four observations; 20140504, 20140712, 20140928 and 20200620, as the reference epoch, t_{ref}. The justification for this is presented in Sec. 3.4. For $t = t_{ref}$, $F_{scale}(\nu,\ t)$ is considered as

$F_{ref}(\nu)$, which is similar to that defined in Sec. 2.2 as,

$$F_{ref}(\nu) = F_{scale}(\nu, t = t_{ref})$$
$$F_{ref}(\nu) = \frac{1}{A_{ref}(\nu) \, |G_{mean,ref}|^2 \, |B_{inter}(\nu)|^2}$$
$$F_{ref}(\nu) = \frac{1}{A_{ref}(\nu) \, |B_{ref}(\nu)|^2} \quad (6)$$
$$F_{ref}(\nu) = \frac{F_{cat}(\nu)}{F_{app,ref}(\nu)}$$

where, $B_{ref}(\nu) = G_{mean,ref}B_{inter}(\nu)$ is the un-normalised inter picket bandpass gain without attenuation, $G_{mean,ref}$ is the $G_{mean}(t)$ for $t = t_{ref}$ and $F_{app,ref}(\nu)$ is the apparent flux densities of the background sources for t_{ref}. The time variations in $F_{scale}(\nu, t)$ arise due to those in $G_{mean}(t)$. These time variations are computed by comparing the instrumental bandpass gain amplitudes for any epoch, t, with the overlapping frequency of the $B_{ref}(\nu)$. For most MWA solar observations, the calibrator observations were done without the use of attenuators. When applying the bandpass calibration to solar data, we also need to take the additional attenuation into account and that is done using $F_{scale}(\nu, t)$.

3.2.2. Computing flux scale polynomials

In this section we discuss the recipe for computing $F_{ref}(\nu)$ and $B_{ref}(\nu)$. Left panel of Fig. 6 shows the variation of $F_{ref}(\nu)$, obtained using different datasets and approaches, as a function of frequency, following the Eq. 6 using $F_{cat}(\nu)$ and $F_{app,ref}(\nu)$ as described in Sec. 2.2. The frequency dependence of $F_{ref}(\nu)$ comes from the overall bandpass response of the MWA. The uncertainty on each of the measurements were obtained by adding $\Delta F_{ref}(\nu)$ and the 8% systematic flux density uncertainty of the GLEAM survey for the sources in the declination (δ) range $-72° \leq \delta \leq 18.5°$ (Hurley-Walker et al. 2017) in quadrature. It is evident that $F_{ref}(\nu)$ varies smoothly across the MWA observing band. The $F_{ref}(\nu)$ values obtained on 20140928 are systematically higher as compared to other days. We note that the attenuator setting used on this day was higher (14 dB) than what was used on the other three days (10 dB) and return to a discussion of these observations later in this section. Till then we focus on the observations made with 10 dB attenuation.

Since calibrator observation of VirgoA with and without the attenuator was only available for 2014 July 12, and two close by epochs, 2014 July 11 and 2014 July 13, we have used these epochs to determine $B_{ref}(\nu)$. These calibrator observations were done in contiguous mode at 140–170 and 170–200 MHz. The direction independent bandpass for these two calibrator observa-

tions was estimated following the method described in Sokolowski et al. (2017). A mean instrumental gain amplitude has been computed for these observations by averaging over all antennas and both the polarization. An average instrumental bandpass gain, $B_{tot}(\nu, t_{ref}) = G_{mean}(t_{ref})B_{inter}(\nu) = G_{mean,ref}B_{inter}(\nu)$, spanning the entire MWA band was similarly computed using 20140712 VirgoA observations, which were done using 10 dB attenuation. We assume the instrumental gain amplitudes, $G_{mean}(t)$, are similar for the calibrator observations on these close epochs. A ratio of $|G_{mean}|^2$, with and without attenuation, has been computed using the overlapping parts of the band. The ratio has been found to be $r \sim 0.09 \pm 0.003$. Though the attenuators are calibrated in power units (squared of the voltage), in the MWA signal chain, the attenuation is applied to the analog voltages. Hence, for 10 dB attenuation we expect a change in $|G_{mean}|^2$ by a factor of 0.1. The ratio r is reassuringly close to the expected value. This suggests that for the observations done with 14 dB attenuation r is likely to lie close to its expected value of 0.04. We use the amplitudes of $B_{tot}(\nu, t_{ref})$ obtained using observations on 2014 July 11 and 2014 July 13 and scaled by the factor of $\sqrt{r}$ just determined, as the amplitude of $B_{ref}(\nu)$. It is shown in the right panel of Fig. 6 and reflects the MWA spectral response across the band.

To make it convenient to use $F_{ref}(\nu)$ and amplitudes of $B_{ref}(\nu)$ for any given frequency, we fit the observed values of $F_{ref}(\nu)$ and the amplitudes of $B_{ref}(\nu)$ with a polynomial. A 5th order polynomial is found to provide a good fit.

$$y = a_5\nu^5 + a_4\nu^4 + a_3\nu^3 + a_2\nu^2 + a_1\nu + a_0 \quad (7)$$

where y is either $F_{ref}(\nu)$ or the amplitudes of $B_{ref}(\nu)$. The best fit polynomials are shown in Fig. 6 and the polynomial coefficients are listed in Table 2.

All of the MWA solar observations thus far have used one of two attenuation settings discussed here – 10 dB and 14 dB. The observations with 14 dB attenuation used here cover only the part of the MWA band below ~ 133 MHz. The ratio of the $F_{ref}(\nu)$ values obtained at 10 and 14 dB are remarkably consistent with each other at all frequencies $\lesssim 133$ MHz, with both the mean and median of these numbers being ~ 1.19 and the standard deviation is 0.07. To be able to extend the $F_{ref}(\nu)$ for 14 dB to the rest of the MWA band we take the empirical approach of scaling the best fit polynomial for $F_{ref}(\nu)$ arrived at for 10 dB observations by a factor of 1.19. Similarly, $|B_{ref}(\nu)|^2$, determined for 10 dB, needs to be multiplied by $0.04/0.1 = 0.4$ for 14 dB observations.

Note that, due to inaccuracies in the primary beam model the observed flux densities can show system-

Polynomial coefficient	$F_{ref}(\nu)$	$amp\ (B_{ref})$
$a_5 \times 10^9$	-1.462 ± 0.009	-0.7070 ± 0.029
$a_4 \times 10^6$	$+1.558 \pm 0.078$	$+0.5216 \pm 0.017$
$a_3 \times 10^4$	-6.250 ± 0.024	-1.4825 ± 0.005
$a_2 \times 10^1$	$+1.207 \pm 0.036$	$+0.2032 \pm 0.007$
$a_1 \times 10^{-1}$	-1.159 ± 0.026	-0.1350 ± 0.005
$a_0 \times 10^{-2}$	$+4.719 \pm 0.076$	$+0.3449 \pm 0.015$

Table 2. Best fit value of polynomial coefficients used in Figure 6. ν is in MHz.

atic declination and frequency dependent biases (Sutinjo et al. 2015; Hurley-Walker et al. 2017). For the purpose of arriving at the best fit polynomial, we ignore these systematic errors and only take the random errors into account.

3.3. *Variation of instrumental gain in time*

A database of MWA calibration solutions has recently been made available by Sokolowski et al. (2020). This database provides robust amplitude and phase calibration solutions for individual antenna tiles at multiple epochs per day for a large fraction of MWA data available at the data archive hosted by the Pawsey Supercomputing Centre via the MWA ASVO interface[2]. We use this database to estimate the stability of $B_{inter}(\nu)$ in time and the variation of $G_{mean}(t)$ seen in the MWA data. For this exercise, calibration solutions were chosen from this database at intervals of two to three weeks spanning the period from June 2013 to June 2020 and a normalized bandpass, $B_{inter}(\nu)$, was computed for each epoch. The 1σ variation of the amplitude of the $B_{inter}(\nu)$ was found to lie in the range of 4–5% at edges of the MWA band and 2–3% in the middle part of the MWA band. The variation in the amplitude of $B_{inter}(\nu)$ is comparable to the ~3% uncertainty in the $F_{ref}(\nu)$ and that on its best fit polynomial description. It is also much smaller than the ~8% uncertainty associated with GLEAM absolute flux density calibration. This implies that the epoch-to-epoch variations in the spectral shape of the $B_{inter}(\nu)$ lead to an insignificant increase in the overall uncertainty in absolute flux density calibration. On the other hand, $G_{mean}(t)$ shows much larger variations of 10–30% from epoch to epoch. This needs to be corrected to avoid leaving a large systematic uncertainty in the absolute flux density estimates.

3.4. *Stability of attenuator response*

[2] https://asvo.mwatelescope.org/

For t_{ref} we get from Eq. 6,

$$F_{ref}(\nu)\ |B_{ref}(\nu)|^2 = \frac{1}{A_{ref}(\nu)} \qquad (8)$$

We show the product of $F_{ref}(\nu)$ and $|B_{ref}(\nu)|^2$ in Fig. 7. As is evident from this figure, it does not show a systematic trend with frequency and has a mean and rms of 44 and 4 respectively for 10 dB attenuation. The scatter observed in this quantity is much smaller than the fractional systematic variations across the band seen in either of $F_{ref}(\nu)$ and $B_{ref}(\nu)$. This implies, that $A_{ref}(\nu)$ does not have a significant spectral dependence. This frequency independence can be made use of for flux density calibration of the solar observations even when calibrator observations in same spectral settings are not available. We can use any calibrator observation to determine the un-normalised bandpass gain, $B_{tot}(\nu, t) = G_{mean}(t)\ B_{inter}(\nu, t)$. The stability of spectral shape of the $B_{inter}(\nu)$, as discussed in Sec. 3.3, allow us to take the same $B_{inter}(\nu)$ for both t and t_{ref}. We determine the value of the scaling, $S(t)$ as,

$$\begin{aligned} S(t) &= \frac{|B_{ref}(\nu)|^2}{|B_{tot}(\nu, t)|^2} \\ &= \frac{|G_{mean,ref}|^2\ |B_{inter}(\nu)|^2}{|G_{mean}(t)|^2\ |B_{inter}(\nu)|^2} \\ &= \frac{|G_{mean,ref}|^2}{|G_{mean}(t)|^2} \end{aligned} \qquad (9)$$

$B_{ref}(\nu)$ is needed to obtain the $S(t)$ from any calibrator observation without attenuation in any spectral configuration to scale the $F_{ref}(\nu)$ to $F_{scale}(\nu,\ t)$.

Consistency of $F_{ref}(\nu) = F_{scale}(\nu,\ t = t_{ref})$ over reference epochs has been demonstrated in left panel of Fig. 6. $F_{scale}(\nu,\ t)$ has contributions from both attenuator response and instrumental gain. Though it is likely that the consistency of $F_{scale}(\nu,\ t)$ across epochs arises from the individual stability of both the bandpass amplitude or the attenuator response. Thus one cannot formally claim this due to the degeneracy just mentioned. An independent estimate for the stability of the attenuator response can be arrived at by exploring the stability of the bandpass amplitude solutions for these epochs. The bandpass amplitudes for those of the epochs shown in Fig. 8 for which calibrator observations without any additional attenuation are available. The data quality of 2014 September 27 was poorer for frequencies greater than 150 MHz and is not shown here. These mean bandpass amplitudes show that even data taken months apart are consistent within ~2%. This is very similar to the variability observed in $F_{scale}(\nu, t)$ and, hence, implies that the attenuator response must have remained

essentially constant across these observations. This is consistent with the expectations that, being passive devices, attenuators are not prone to significant evolution in their characteristics and suggests that it is reasonable to assume that the attenuator performance, $A(t)$, has remained steady across time. We did not have any calibrator observations with the same frequency range as shown in Fig. 8 for 2020 June 20. Thus we could not directly compare the bandpass amplitude with the other three epochs. Since the $F_{scale}(\nu, t)$ for 2020 June 20 also well matched with other epochs and the time independent nature of A just mentioned, we have considered 2020 June 20 also as a reference epoch. Since A is independent of time and frequency, we could use the scaling values for $F_{ref}(\nu)$ and $B_{ref}(\nu)$ from 10 dB to 14 dB as mentioned in Sec. 3.3 for any other epochs. Using Eq. 6 and scaling values mentioned in Sec. 3.3, we obtain the value of $\frac{1}{A}$ for 14 dB attenuation is 92.

3.5. A comparison with GLEAM

It is instructive to compare the image presented in Section 3.1 with the typical imaging quality delivered by the MWA GLEAM survey (Hurley-Walker et al. 2017), as it provides a good benchmark for quality of imaging being provided by our solar imaging pipeline (Kansabanik D. et al., in preparation). At 108 MHz, using 20140504 data we obtain an image rms of ~ 0.72 Jy for an integration time of 2 minutes and 2.28 MHz bandwidth. The GLEAM survey lists typical rms values at 72 MHz and 240 MHz for its integration time of 2 minutes and bandwidth of 7.68 MHz. Using this information, we estimate the rms at 108 MHz to be about 0.150 Jy. In addition to the differences in time and frequency integration, an apples-to-apples comparison requires us to also take two other considerations into account. First is the increase in system temperature due to the Sun and this information is available in Oberoi et al. (2017). The second is that being an aperture array, the sensitivity of the MWA is a function of the elevation of the pointing direction, which then also needs to be accounted for. While the GLEAM observations were carried out at the highest elevation feasible for a given declination strip, the 20140504 observations were carried out at the elevation limit of the MWA. Once all these factors are taken into account, it leads to an expected rms of ~ 0.48 Jy for a time and frequency integration of 2 minutes and 2.28 MHz. This demonstrates that, despite the dynamic range limitations expected due to presence of a very bright and extended source in the FoV, our imaging pipeline is able to achieve a rms noise only ~ 1.5 times that expected from extrapolation from GLEAM.

Details of the calculation of sensitivities are presented in Appendix A.

4. APPLYING THE FLUX SCALE

For the MWA solar observations, the following prescription can be used to obtain absolute flux density calibrated images in units of Jy/beam:

1. Compute normalized bandpass, $B_{picket}(\nu)$, for each 1.28 MHz coarse channel for the solar observations independently and correct for it.

2. Correct the solar images for the primary beam response using the full embedded element beam model (Sokolowski et al. 2017) for every 1.28 MHz coarse channel.

3. Compute the value of $F_{ref}(\nu)$ and $B_{ref}(\nu)$ corresponding to the value of attenuation used for the observation (10 dB or 14 dB) using the polynomial coefficients in Table 2 at the desired observing frequency.

4. Obtain bandpass gains for any calibrator observation, $B_{tot}(\nu, t)$, in any spectral configuration without any additional attenuation from a nearby epoch. Compute $S(t)$ from Eq. 9 using the part of the band overlapping between $B_{tot}(\nu,t)$ and $B_{ref}(\nu)$.

5. Since A is considered to be independent of time and frequency, $A(\nu, t) = A_{ref}(\nu) = A$. From Equations. 5, 6 and 9, $F_{scale}(\nu, t)$ for any observing epoch, t, can be written as,

$$
\begin{aligned}
F_{scale}(\nu, t) &= \frac{1}{A\ |B_{tot}(\nu, t)|^2} \\
&= \frac{1}{A\ |G_{mean}(t)|^2\ |B_{inter}(\nu)|^2} \\
&= \frac{S(t)}{A\ |G_{mean,ref}|^2\ |B_{inter}(\nu)|^2} \quad (10) \\
&= \frac{S(t)}{A\ |B_{ref}(\nu)|^2} \\
F_{scale}(\nu, t) &= S(t)\ F_{ref}(\nu)
\end{aligned}
$$

6. Multiply the primary beam corrected solar images with $F_{scale}(\nu, t)$ to obtain the final flux density calibrated image in Jy/beam units. $F_{scale}(\nu, t)$ corrects the MWA bandpass response, temporal variation of the instrumental gain and the response of the attenuator.

7. An approximate way to account for the uncertainties due to multiple contributions is to add, in

quadrature, an additional 10% uncertainty to the values obtained from the best fit polynomial.

This method can also be employed for solar observations with no corresponding calibrator observations, as was the case during early solar observations with the MWA. It has the ability to correct for the large variation in the overall amplitude of the frequency independent gain of the MWA bandpass, which would otherwise be the dominant source uncertainty, using $S(t)$. The uncertainty in the $F_{scale}(\nu, t)$ come primarily from the $\sim$8% uncertainty of GLEAM flux densities, 3–4% uncertainty on $F_{ref}(\nu)$ due to the thermal noise and the 2–5% variations in the bandshape across epochs. Together, they lead to an overall uncertainty of $\sim$10% in the final flux density estimates.

5. CONCLUSION

We describe a robust flux density calibration method for solar observations with the MWA. Not only is the $\sim$10% uncertainty it delivers is a significant improvement over the 10–60% uncertainty provided by technique in use thus far (Oberoi et al. 2017), the intrinsic simplicity of its application also makes it much less compute intensive than the earlier approach. There are also multiple other significant limitations of the earlier technique which this method overcomes.

The limitations overcome include the requirement of a sufficient number of very short baselines; and the dependence of the uncertainty in flux density calibration on the location of the Sun in the sky and the state of solar emission. This method can also be applied to any solar observations done with MWA independent of array configuration, spectral configuration and attenuator settings. Only two different attenuation settings have been used for MWA solar observations, and the scaling between them has also been determined here. The method can also provide flux density calibration for solar data even for the epochs without any matching calibrator observations. This approach has been incorporated in the new version of AIRCARS (Kanabanik D. et al., in preparation) and will enable routine generation of solar radio images in absolute flux density units.

We find that MWA sensitivity is sufficient to observe some of the stronger flux density calibrators using the attenuation typically used for solar observations even at our highest observing frequency of 240 MHz. This will be a good practice to follow for future solar observations. Being able to do so will simplify flux density calibration process and will also allow us to take into account any variations in the spectral behavior of $F_{ref}(\nu)$ at scales too fine to be captured by the polynomial fit employed here, if present. This small scale variations in bandpass amplitudes are evident from Fig. 8. Understanding and modeling these small scale variations will be important for characterising the spectral properties of weak non-thermal emissions like the Weak Impulsive Narrow Band Quiet Sun Emissions (WINQSEs; Mondal et al. 2020a; Mondal 2021, Mondal S. et al., in preparation).

This work also demonstrates that the imaging quality delivered by the combination of MWA data and AIRCARS is sufficient to detect multiple background sources in the vicinity of the Sun. The flux density of the weakest source detected here is $\sim$ 4.6 Jy. We detect the closest source at 20 $R_{\odot}$ from the Sun having a flux density of 4.9 Jy. This combined with the large MWA FoV is expected to enable many new capabilities/ studies which have remained inaccessible till now. For instance, the catalogue positions of background sources can be used to improve the astrometric accuracy of solar images. Though one will still have coronal propagation effects to contend with, this will be step forward on the long standing issue which arises because the locations of coronal radio features do not correspond precisely to photospheric or chromospheric features. This work also suggests that it will be interesting to explore the possibility of conducting interplanetary scintillation (IPS) observations with the Sun in the FoV. Currently IPS observations with the MWA are conducted while keeping the Sun in a null of the MWA beam (e.g. Morgan et al. 2018; Chhetri et al. 2018). The large angular size of the Sun and the chromatic nature of the MWA beams, however, severely restrict the observing windows both in time and also frequency, which this approach might help overcome. Combined with wide FoV polarimetric imaging, the ability to see multiple faint background sources can be used to perform image-based polarisation leakage correction. This is also an essential step towards developing the ability to measure the Faraday rotation of linearly polarized radiation from background sources due to the magnetised CME plasma, a long term goal which we are pursuing.

APPENDIX

A. COMPARISON OF IMAGE RMS NOISE WITH GLEAM SURVEY

This appendix presents the calculations of the expected rms noise for 20140504 observation and its comparison with the GLEAM survey (Hurley-Walker et al. 2017). Expected rms noise per polarisation, $\Delta F_{X,Y}$, can

be written as,

$$\Delta F_{X,Y} = \frac{SEFD_{X,Y}}{\sqrt{N_{ant}(N_{ant}-1)\Delta\nu\Delta t}} \quad (A1)$$

where, X and Y refer to the two orthogonal polarizations, $SEFD$ is the system equivalent flux density, N_{ant} is the number of antennas used for imaging, Δt is the total integration time used for imaging and $\Delta\nu$ the total imaging bandwidth (Thompson et al. 2017). $SEFD$ can also be expressed in terms of effective collecting area, A_{eff}, and system temperature, T_{sys}, as,

$$SEFD = \frac{2\,K\,T_{sys}}{A_{eff}}, \quad (A2)$$

where K is the Boltzmann constant (Thompson et al. 2017). The A_{eff} has been calculated using the Full Embedded Element primary beam model developed by Sokolowski et al. (2017). T_{sys} has the contributions from beam averaged sky temperature (T_{sky}), receiver temperature (T_{rec}) and ground pick up (T_{pick}). We use values of T_{rec} and T_{pick} provided by Ung et al. (2020).

GLEAM observations were done using the primary beam pointings at higher elevations. For aperture arrays like the MWA, the sensitivity is a function of elevation and higher elevations offer greater sensitivity. We choose a GLEAM pointing at 108 MHz for the same part of the sky as 20140504 solar observation. The theoretical thermal rms noise of GLEAM image, without any contribution from the Sun, was calculated using Eqs. A1 and A2 and the parameters listed in Table A. The theoretical rms noise for GLEAM was estimated to be ∼38 mJy. The noise obtained in the GLEAM images is ∼150 mJy (Hurley-Walker et al. 2017), ∼4 times larger than the theoretical value.

To estimate the theoretical thermal rms for solar images, we add the beam averaged contribution of the Sun ($T_{\odot}$) to the T_{sys}. $T_{\odot}$ at 108 MHz was estimated to be 159 K and represents the average of the values at 103 and 117 MHz from Oberoi et al. (2017), which provides the values for a quiet solar time. In addition, while the GLEAM survey in general used a full 128 MWA antenna elements (tiles), only 115 of them were used for observations on 20140504. Taking these considerations into account leads to a theoretical thermal noise of 120 mJy for solar observations on 20140504 using the parameters mentioned in Table A. Scaling up the thermal noise by the factor of 4 estimated for GLEAM leads to an expectation of 480 mJy for the observed rms noise. The

actual value of the rms observed in solar map is 720 mJy, a factor 1.5 higher than the expectations based on GLEAM.

Facilities: Murchison Widefield Array (MWA) (Lonsdale et al. 2009; Tingay et al. 2013)

Software: astropy (Price-Whelan et al. 2018), matplotlib (Hunter 2007), Numpy (Harris et al. 2020), CASA (McMullin et al. 2007), PyBDSF (Mohan & Rafferty 2015), AIRCARS (Mondal et al. 2019)

REFERENCES

Avignon, Y., Bonmartin, J., Bouteille, A., et al. 1989, SoPh, 120, 193

Bastian, T. S., Pick, M., Kerdraon, A., Maia, D., & Vourlidas, A. 2001, ApJL, 558, L65, doi: 10.1086/323421

Observation	$A_{eff,X}$ (m^2)	$A_{eff,Y}$ (m^2)	$SEFD_X$ (Jy)	$SEFD_Y$ (Jy)	$T_{sky,X}$ (K)	$T_{sky,Y}$ (K)	$T_{\odot}$ (K)	$T_{sys,X}$ (K)	$T_{sys,Y}$ (K)	$\Delta\nu$ (MHz)	Δt (s)
GLEAM	17.33	13.98	134098	160703	731	703	0	842	814	7.68	120
20140504	11.61	11.69	230594	226891	700	691	159	970	961	2.28	120

Table 3. Parameters used to estimate the theoretical rms noise.

* We have used $T_{rec} = 91$ K and $T_{pick} = 20$ K.

Bell, M. E., Murphy, T., Kaplan, D. L., et al. 2013, Monthly Notices of the Royal Astronomical Society, 438, 352, doi: 10.1093/mnras/stt2200

Bonmartin, J., Bouteille, A., Clavelier, B., et al. 1983, SoPh, 88, 383, doi: 10.1007/BF00196201

Bonnarel, F., Fernique, P., Genova, F., et al. 1999, in Astronomical Society of the Pacific Conference Series, Vol. 172, Astronomical Data Analysis Software and Systems VIII, ed. D. M. Mehringer, R. L. Plante, & D. A. Roberts, 229

Breitling, F., Mann, G., Vocks, C., Steinmetz, M., & Strassmeier, K. G. 2015, Astronomy and Computing, 13, 99, doi: 10.1016/j.ascom.2015.08.001

Carley, E. P., Vilmer, N., Simões, P. J. A., & Ó Fearraigh, B. 2017, A&A, 608, A137, doi: 10.1051/0004-6361/201731368

Chhetri, R., Morgan, J., Ekers, R. D., et al. 2018, MNRAS, 474, 4937, doi: 10.1093/mnras/stx2864

Gibson, S., Kucera, T., White, S., et al. 2016, Frontiers in Astronomy and Space Sciences, 3, 8, doi: 10.3389/fspas.2016.00008

Harris, C. R., Millman, K. J., van der Walt, S. J., et al. 2020, Nature, 585, 357, doi: 10.1038/s41586-020-2649-2

Haslam, C. G. T., Salter, C. J., Stoffel, H., & Wilson, W. E. 1982, A&AS, 47, 1

Helmboldt, J. F., & Hurley-Walker, N. 2020, Radio Science, 55, e07106, doi: 10.1029/2020RS007106

Hunter, J. D. 2007, Computing in Science & Engineering, 9, 90, doi: 10.1109/MCSE.2007.55

Hurley-Walker, N., & Hancock, P. J. 2018, Astronomy and Computing, 25, 94, doi: 10.1016/j.ascom.2018.08.006

Hurley-Walker, N., Callingham, J. R., Hancock, P. J., et al. 2017, MNRAS, 464, 1146, doi: 10.1093/mnras/stw2337

Jordan, C. H., Murray, S., Trott, C. M., et al. 2017, MNRAS, 471, 3974, doi: 10.1093/mnras/stx1797

Kontar, E. P., Yu, S., Kuznetsov, A. A., et al. 2017, Nature Communications, 8, 1515, doi: 10.1038/s41467-017-01307-8

Loi, S. T., Trott, C. M., Murphy, T., et al. 2015, Radio Science, 50, 574, doi: 10.1002/2015RS005711

Loi, S. T., Murphy, T., Cairns, I. H., et al. 2015, Geophysical Research Letters, 42, 3707, doi: https://doi.org/10.1002/2015GL063699

Lonsdale, C. J., Cappallo, R. J., Morales, M. F., et al. 2009, IEEE Proceedings, 97, 1497, doi: 10.1109/JPROC.2009.2017564

Lynch, C. R., Lenc, E., Kaplan, D. L., Murphy, T., & Anderson, G. E. 2017, ApJL, 836, L30, doi: 10.3847/2041-8213/aa5ffd

McCauley, P. I., Cairns, I. H., Morgan, J., et al. 2017, ApJ, 851, 151, doi: 10.3847/1538-4357/aa9cee

McMullin, J. P., Waters, B., Schiebel, D., Young, W., & Golap, K. 2007, in Astronomical Society of the Pacific Conference Series, Vol. 376, Astronomical Data Analysis Software and Systems XVI, ed. R. A. Shaw, F. Hill, & D. J. Bell, 127

Mohan, A. 2021, ApJL, 909, L1, doi: 10.3847/2041-8213/abe70a

Mohan, A., McCauley, P. I., Oberoi, D., & Mastrano, A. 2019a, ApJ, 883, 45, doi: 10.3847/1538-4357/ab3a94

Mohan, A., Mondal, S., Oberoi, D., & Lonsdale, C. J. 2019b, ApJ, 875, 98, doi: 10.3847/1538-4357/ab0ae5

Mohan, A., & Oberoi, D. 2017, SoPh, 292, 168, doi: 10.1007/s11207-017-1193-1

Mohan, N., & Rafferty, D. 2015, PyBDSF: Python Blob Detection and Source Finder. http://ascl.net/1502.007

Mondal, S. 2021, Solar Physics, 296, 131, doi: 10.1007/s11207-021-01877-3

Mondal, S., Mohan, A., Oberoi, D., et al. 2019, ApJ, 875, 97, doi: 10.3847/1538-4357/ab0a01

Mondal, S., Oberoi, D., & Mohan, A. 2020a, ApJL, 895, L39, doi: 10.3847/2041-8213/ab8817

Mondal, S., Oberoi, D., & Vourlidas, A. 2020b, ApJ, 893, 28, doi: 10.3847/1538-4357/ab7fab

Morgan, J. S., Macquart, J. P., Ekers, R., et al. 2018, MNRAS, 473, 2965, doi: 10.1093/mnras/stx2284

Oberoi, D., Sharma, R., & Rogers, A. E. E. 2017, SoPh, 292, 75, doi: 10.1007/s11207-017-1096-1

Perley, R. A., & Butler, B. J. 2017, ApJS, 230, 7, doi: 10.3847/1538-4365/aa6df9

Price-Whelan, A. M., Sipőcz, B., Günther, H., et al. 2018, The Astronomical Journal, 156, 123

Rahman, M. M., McCauley, P. I., & Cairns, I. H. 2019, SoPh, 294, 7, doi: 10.1007/s11207-019-1396-8

Rogers, A. E. E., Pratap, P., Kratzenberg, E., & Diaz, M. A. 2004, Radio Science, 39, RS2023, doi: 10.1029/2003RS003016

Rowlinson, A., Bell, M. E., Murphy, T., et al. 2016, Monthly Notices of the Royal Astronomical Society, 458, 3506, doi: 10.1093/mnras/stw451

Sharma, R., & Oberoi, D. 2020, arXiv e-prints, arXiv:2009.10604. https://arxiv.org/abs/2009.10604

Sharma, R., Oberoi, D., & Arjunwadkar, M. 2018, ApJ, 852, 69, doi: 10.3847/1538-4357/aa9d96

Sokolowski, M., Colegate, T., Sutinjo, A. T., et al. 2017, PASA, 34, e062, doi: 10.1017/pasa.2017.54

Sokolowski, M., Jordan, C. H., Sleap, G., et al. 2020, PASA, 37, e021, doi: 10.1017/pasa.2020.17

Sundaram, G. A. S., & Subramanian, K. R. 2004, ApJ, 605, 948, doi: 10.1086/382582

—. 2005, MNRAS, 359, 580, doi: 10.1111/j.1365-2966.2005.08924.x

Suresh, A., Sharma, R., Oberoi, D., et al. 2017, ApJ, 843, 19, doi: 10.3847/1538-4357/aa774a

Sutinjo, A., O'Sullivan, J., Lenc, E., et al. 2015, Radio Science, 50, 52, doi: 10.1002/2014RS005517

Thompson, A. R., Moran, J. M., & Swenson, George W., J. 2017, Interferometry and Synthesis in Radio Astronomy, 3rd Edition, doi: 10.1007/978-3-319-44431-4

Tingay, S. J., Goeke, R., Bowman, J. D., et al. 2013, PASA, 30, e007, doi: 10.1017/pasa.2012.007

Tun, S. D., & Vourlidas, A. 2013, ApJ, 766, 130, doi: 10.1088/0004-637X/766/2/130

Ung, D. C. X., Sokolowski, M., Sutinjo, A. T., & Davidson, D. B. 2020, IEEE Transactions on Antennas and Propagation, 68, 5395, doi: 10.1109/TAP.2020.2980334

Van Rossum, G., & Drake Jr, F. L. 1995, Python reference manual (Centrum voor Wiskunde en Informatica Amsterdam)

Wayth, R. B., Lenc, E., Bell, M. E., et al. 2015, PASA, 32, e025, doi: 10.1017/pasa.2015.26

Wayth, R. B., Tingay, S. J., Trott, C. M., et al. 2018, PASA, 35, 33, doi: 10.1017/pasa.2018.37